Application of machine learning potentials to predict grain boundary properties in fcc elemental metals

Takayuki Nishiyama [1,*] Atsuto Seko [1,†] and Isao Tanaka [1,2,3]

[1]*Department of Materials Science and Engineering, Kyoto University, Kyoto 606-8501, Japan*
[2]*Center for Elements Strategy Initiative for Structure Materials (ESISM), Kyoto University, Kyoto 606-8501, Japan*
[3]*Nanostructures Research Laboratory, Japan Fine Ceramics Center, Nagoya 456-8587, Japan*

Accurate interatomic potentials are in high demand for large-scale atomistic simulations of materials that are prohibitively expensive by density functional theory (DFT) calculation. In this study, we apply machine learning potentials (MLPs) in a recently constructed repository to the prediction of the grain boundary energy in face-centered-cubic elemental metals, i.e., Ag, Al, Au, Cu, Pd, and Pt. The systematic application of machine learning potentials shows that they enable us to predict grain boundary structures and their energies accurately. The grain boundary energies predicted by the MLPs are in agreement with those calculated by DFT, although no grain boundary structures were included in training datasets of the present MLPs.

I. INTRODUCTION

Grain boundaries are interfaces between differently oriented crystals of the same phase [1]. The microstructures of grain boundaries can affect various properties of polycrystalline materials, including mechanical, thermal, and electrical properties [2–5]. Thus, an attractive topic in materials science has been to establish the relationship between the properties of crystalline materials and grain boundary structures. Many theoretical studies have been done to cover a broad range of grain boundary structures and their excess energies. Early fundamental studies employed pair potentials, such as the Lennard-Jones and Morse forms, to investigate the generic properties of grain boundaries such as the presence of cusps in a map of the rotation angle and the grain boundary energy [6–8]. Empirical interatomic potentials such as the Finnis-Sinclair (FS) potentials [9] and embedded atom method (EAM) [10] potentials have been widely used to investigate symmetric and asymmetric grain boundaries of metallic materials. Quantitative predictions are becoming possible [11–20], and strong correlations between theoretical and experimental grain boundary energies have been shown, especially for grain boundaries in elemental Al and Ni, which exhibit low grain boundary energies [21,22]. However, the prediction error in the grain boundary energy may be significant in grain boundaries showing higher grain boundary energies. This error originates from the fact that their microscopic grain boundary structures differ from the atomic environment used to estimate interatomic potentials.

Density functional theory (DFT) calculation [23,24] is an alternative way to predict grain boundary properties accurately. However, DFT calculation is practically impossible to apply to large-scale models of grain boundaries owing to its computational cost. Therefore, interatomic potentials that enable us to predict grain boundary properties accurately have been in high demand. Over the last decade, many groups have proposed frameworks to develop machine learning potentials (MLPs) based on extensive datasets generated by DFT calculation [25–46]. The MLPs significantly improve the accuracy and transferability of interatomic potentials. Also, MLPs themselves are becoming available, such as those in the Machine Learning Potential Repository [47] developed by one author of this paper.

In this paper, we demonstrate the predictive power of MLPs in the MLP repository for grain boundary properties. We systematically evaluate the structures and excess energies of ⟨100⟩ symmetric tilt grain boundaries (STGBs), ⟨110⟩ STGBs, and ⟨100⟩ pure-twist grain boundaries in the face-centered-cubic (fcc) elemental metals Ag, Al, Au, Cu, Pd, and Pt. They are compared with those obtained from EAM potentials and DFT calculations. The MLP repository contains a set of Pareto optimal MLPs with different tradeoffs between accuracy and computational efficiency; hence, we carefully determine appropriate MLPs to predict grain boundary properties.

II. METHODOLOGY

A. Modeling and structure optimization of grain boundaries

Macroscopic structures of grain boundaries are characterized by five geometrical degrees of freedom. We choose three variables to specify the direction of the rotation axis and the rotation angle, which describe the misorientation between crystal lattices, and two variables to specify the direction of the boundary plane normal [1]. For a given set of macroscopic variables, the microscopic structure is associated with three degrees of freedom regarding rigid body displacements: two components parallel to the boundary plane and one component normal to the plane. Hence, the globally optimal microscopic structure for a given set of macroscopic

_____
*nishiyama.takayuki.84e@st.kyoto-u.ac.jp
†seko@cms.mtl.kyoto-u.ac.jp

variables is achieved by optimizing the three microscopic variables in terms of potential energy.

In this study, we investigate only STGBs and pure-twist grain boundaries. The periodicity of an STGB is identified from the orthogonal projection of its coincident site lattice (CSL) to its boundary plane. Also, the periodicity of a pure-twist grain boundary is given by the orthogonal projection of its displacement shift complete (DSC) lattice to its boundary plane. Therefore, we restrict the ranges of the two in-plane microscopic variables to a domain defined by the periodicity of the grain boundaries.

We explore the globally optimal microscopic structure for a set of macroscopic variables using a multistart method. The multistart method involves local structure optimizations for a given set of initial structures and regards the structure with the lowest energy among the converged final structures as the globally optimal structure. We use the conjugate gradient method implemented in the LAMMPS code [48] for the local structure optimizations. Initial microscopic structures are introduced from a 4×4 grid for the two in-plane components and a sequence for the component normal to the boundary plane. In other words, one crystal is shifted relative to the other crystal by a vector identified with an in-plane grid point and a value from the sequence for the normal component. For each initial microscopic structure, a calculation model is generated using PYMATGEN [49]. This model contains two parallel boundaries perpendicular to the c axis of the model, separated by fcc layers corresponding to four repetitions of a cell of the CSL. However, the local structure optimization starting from some of the initial microscopic structures fails to converge when using both the MLPs and the EAM potentials, as shown in the next section. These structures are ignored in finding the globally optimal microscopic structure. Note that the optimization of the microscopic structure is performed in the whole domain here, although it is more efficient to restrict the domain to its symmetrically nonequivalent domain.

B. Machine learning potentials

We employ MLPs in the Machine Learning Potential Repository [47] developed by one author of this paper to obtain the globally optimal microscopic structures of STGBs and pure-twist grain boundaries. In the repository, a set of Pareto optimal MLPs with different tradeoffs between accuracy and computational efficiency is available, from which one can choose an appropriate MLP in accordance with the target and purpose. Potential energy models of the MLPs are either a polynomial model of Gaussian-type pairwise structural features or a polynomial model of polynomial invariants for the O(3) group, which are derived by a group-theoretical approach [50]. A brief description of the potential energy models and the structural features used for developing the MLPs is given in Appendix A.

The Pareto optimal MLPs in the repository have been developed using a dataset generated from structure generators. For Ag, Al, Au, and Cu, we adopt the Pareto optimal MLPs developed from a structure generator set composed of the fcc, body-centered-cubic (bcc), hexagonal-close-packed (hcp), simple cubic (sc), ω, and β tin structures. The dataset is composed of 3000 structures constructed by introducing

random lattice expansion, random lattice distortion, and random atomic displacements into a supercell of the equilibrium structure for one of the structure generators. For Pd and Pt, we employ another set of 82 prototype structures as the structure generator set because the dataset derived from the six structure generators is not available in the repository. The dataset consists of 10 000 structures generated by the same procedure as above. For all structures in the dataset, DFT calculations were performed using the plane-wave-basis projector augmented wave method [51] within the Perdew-Burke-Ernzerhof exchange-correlation functional [52] as implemented in the VASP code [53–55]. Note that the datasets contain no structures generated from grain boundary models.

III. RESULTS AND DISCUSSION

First, we choose an accurate MLP requiring only a reasonable computational time to investigate the whole set of grain boundaries. A practical approach to selecting an MLP from the whole set of Pareto optimal MLPs is to find an MLP with high computational cost performance in terms of the prediction error for a test dataset. It can be obtained from the distribution of Pareto optimal MLPs shown in Appendix B. Another practical approach is to examine the convergence behavior of the target property in terms of the computational cost using the whole set of Pareto optimal MLPs. We adopt the latter approach to select an MLP in this study. Therefore, we systematically calculate the grain boundary energies of five grain boundaries using the whole set of Pareto optimal MLPs for each elemental metal. They are the $\Sigma 5 \langle 100 \rangle$ STGB (at 53.1°), the $\Sigma 3 \langle 110 \rangle$ STGB (at 70.5°), the $\Sigma 3 \langle 110 \rangle$ STGB (at 109.5°), the $\Sigma 9 \langle 110 \rangle$ STGB (at 38.9°), and the $\Sigma 5 \langle 100 \rangle$ pure-twist grain boundary (at 36.9°), the calculation models for which can be represented by a small number of atoms.

Figure 1 shows the convergence behavior of the grain boundary energy in terms of the computational time, obtained using the whole set of Pareto optimal MLPs. The grain boundary energy is identical to the lowest energy among the grain boundary energies of the microscopic structures. The grain boundary energy of a microscopic structure is measured from the energy of the equilibrium fcc structure. The computational time corresponding to the model complexity of an MLP is the elapsed time normalized by the number of atoms for a single point calculation of the energy, the forces, and the stress tensors [56]. As can be seen in Fig. 1, the grain boundary energy converges well in all of the elemental metals and grain boundaries. Consequently, successive calculations for the whole set of grain boundaries are performed using the MLP that requires the lowest computational time among the MLPs showing convergence.

Table I lists the model parameters of the selected MLPs. As a consequence of the convergence behavior, fast MLPs are selected for Ag and Cu, while computationally expensive MLPs are selected for the others. Table I also shows the prediction errors for the datasets used in developing the MLPs. The MLPs for Pd and Pt show significant prediction errors, which originate from the fact that the datasets contain many hypothetical structures such as the graphite-type structure. Although the selected MLPs exhibit significant prediction errors for such abnormal structures, they show much smaller
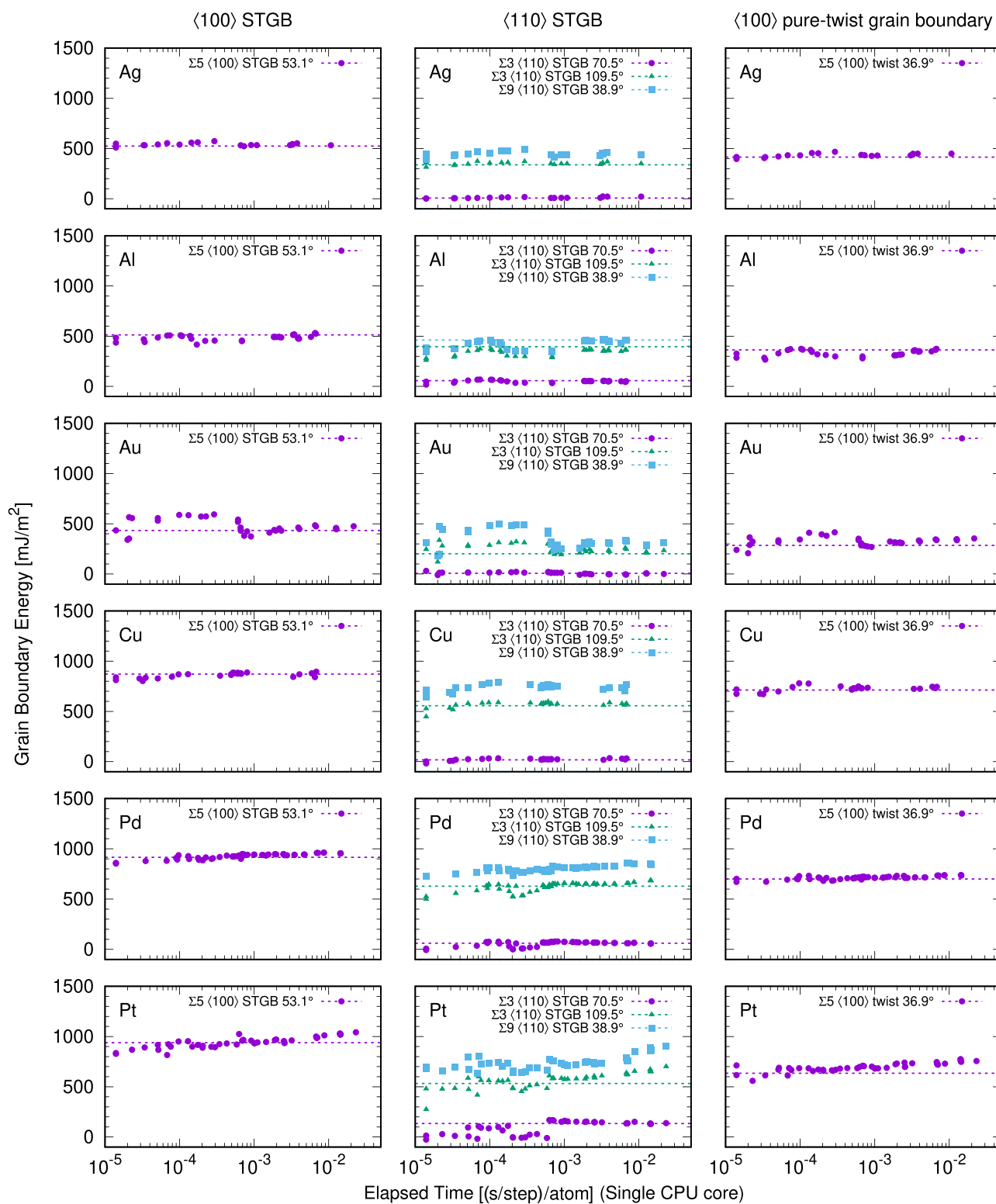
FIG. 1. Grain boundary energies of $\Sigma 5$ $\langle 100 \rangle$ STGB at 53.1°, $\Sigma 3$ $\langle 110 \rangle$ STGB at 70.5°, $\Sigma 3$ $\langle 110 \rangle$ STGB at 109.5°, $\Sigma 9$ $\langle 110 \rangle$ STGB at 38.9°, and $\Sigma 5$ $\langle 100 \rangle$ pure-twist grain boundary at 36.9° for elemental Ag, Al, Au, Cu, Pd, and Pt, predicted using the Pareto optimal MLPs. The grain boundary energies computed by DFT calculation are also shown by broken lines.

prediction errors for typical metallic structures, including grain boundary structures, as shown above.

We also examine the transferability of the MLPs to the prediction of the grain boundary structures and energies because the datasets used in developing the MLPs contain no grain boundary structures. Therefore, we evaluate the grain boundary energies of the $\Sigma 3$ $\langle 110 \rangle$ STGB (at 70.5°), the $\Sigma 3$ $\langle 110 \rangle$ STGB (at 109.5°), the $\Sigma 9$ $\langle 110 \rangle$ STGB

TABLE I. Model parameters of the MLPs used to estimate the grain boundary structures and energies. The identification of the feature type, the model type, and the polynomial orders can be found in Appendix A.

	Ag	Al	Au	Cu	Pd	Pt
MLP-ID	pair-44	gtinv-336	gtinv-111	pair-23	gtinv-722	gtinv-533
RMSE (energy) (meV/atom)	2.2	0.8	0.7	2.2	6.3	12.9
RMSE (force) (eV/Å)	0.010	0.008	0.012	0.013	0.097	0.172
Time (ms/step)/atom [56]	0.05	1.85	0.66	0.04	0.52	0.63
Number of coefficients	815	1100	475	285	500	1595
Feature type	Pair	Invariants	Invariants	Pair	Invariants	Invariants
Cutoff radius (Å)	7.0	8.0	6.0	7.0	6.0	6.0
Number of radial functions	15	15	10	10	5	5
Model type	2	3	3	2	4	2
Polynomial order (function F)	3	3	3	3	2	2
Polynomial order (invariants)		3	3		3	3
Spherical harmonics truncation $\{l_{max}^{(2)}, l_{max}^{(3)}\}$		[4, 4]	[4, 4]		[4, 0]	[4, 2]

(at 38.9°), the Σ5 ⟨100⟩ STGB (at 53.1°), and the Σ5 ⟨100⟩ pure-twist grain boundary (at 36.9°) by DFT calculation, and compare them with those predicted using the MLPs. Figure 1 shows the DFT values of the grain boundary energy only for the grain boundary structures, DFT calculations for which converge successfully [57]. They are close to the grain boundary energies of the selected MLPs. Therefore, the selected MLPs should have high predictive power for grain boundary structures and their energies even though no grain boundary structures were used to develop the MLPs.

After confirming the transferability of the MLPs, we calculate the energies of the grain boundary structures: ⟨100⟩ STGBs (Σ5, Σ13, Σ17, Σ25, Σ29, Σ41), ⟨110⟩ STGBs (Σ3, Σ9, Σ11, Σ17, Σ19, Σ27, Σ33, Σ41, Σ43), and ⟨100⟩ pure-twist grain boundaries (Σ5, Σ13, Σ17, Σ25, Σ29, Σ37, Σ41). Most of them are represented by large-scale models, hence they cannot be calculated by DFT calculation because of the large computational resources required. The number of atoms included in the grain boundaries ranges from 96 to 2112. Figure 2 shows the optimized STGB structures of some STGBs in Ag. Figure 3 shows the rotation angle dependence of the grain boundary energy obtained using the MLPs and EAM potentials [58–63]. The values of the grain boundary energy in Al, Cu, and Pd computed using the MLPs are consistent with those computed using the EAM potentials and those computed by DFT calculation. Therefore, both the MLPs and the EAM potentials have high predictive power for the grain boundary structures and their energies. In Ag, Au, and Pt, the values of the grain boundary energy computed using the MLPs are almost the same as those computed by DFT calculation, whereas they deviate from those computed using the EAM potentials. The MLPs should be more reliable

than the EAM potentials for obtaining not only the grain boundary structures and their energies but also the other defect structures in Ag, Au, and Pt. Note that a fine sequence is required for the component normal to the boundary plane to obtain converged microscopic structures when using the EAM potentials for Ag and Au. This implies that the EAM potentials for Ag and Au lack accuracy for predicting the potential energy surface around the globally optimal microscopic structure.

For every grain boundary, the grain boundary energies in Cu, Pd, and Pt are higher than those in Ag, Al, and Au, as shown in Fig. 3. This trend can be qualitatively understood by considering a simple approximation within the elasticity theory. Using the Read-Shockley equation [65], the shear stress component of the grain boundary energy is obtained by integrating the contributions of dislocations distributed evenly on the interface. Given the shear modulus G and cubic lattice constant a, the excess energies of grain boundaries are approximately proportional to a coefficient Ga. By employing the Voigt averages calculated from the elastic constants of single crystals [66], the coefficients for Ag, Al, Au, Cu, Pd, and Pt are estimated as 1.3, 1.0, 1.2, 1.8, 1.8, and 2.2, respectively, which are normalized by the coefficient for Al. They can be classified into two groups, which is consistent with the grain boundary energy trend.

IV. CONCLUSION

We have examined the predictive power of MLPs in an MLP repository for grain boundary properties by systematically evaluating the grain boundary energy for ⟨100⟩ STGBs, ⟨110⟩ STGBs, and ⟨100⟩ pure-twist grain boundaries in the
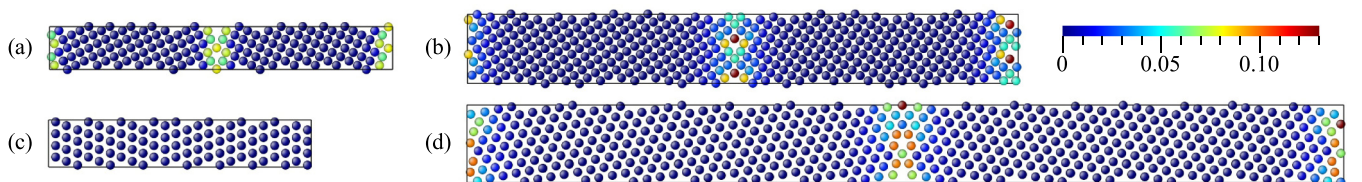
FIG. 2. Optimized structures of (a) Σ5 ⟨100⟩ STGB (at 53.1°), (b) Σ13 ⟨100⟩ STGB (at 67.3°), (c) Σ3 ⟨110⟩ STGB (at 70.5°), and (d) Σ33 ⟨110⟩ STGB (at 20.0°) in Ag. They are represented by 160, 416, 96, and 1056 atoms, respectively. They are visualized using ATOMEYE [64], and colors are assigned to atoms according to their local von Mises shear strain invariant.
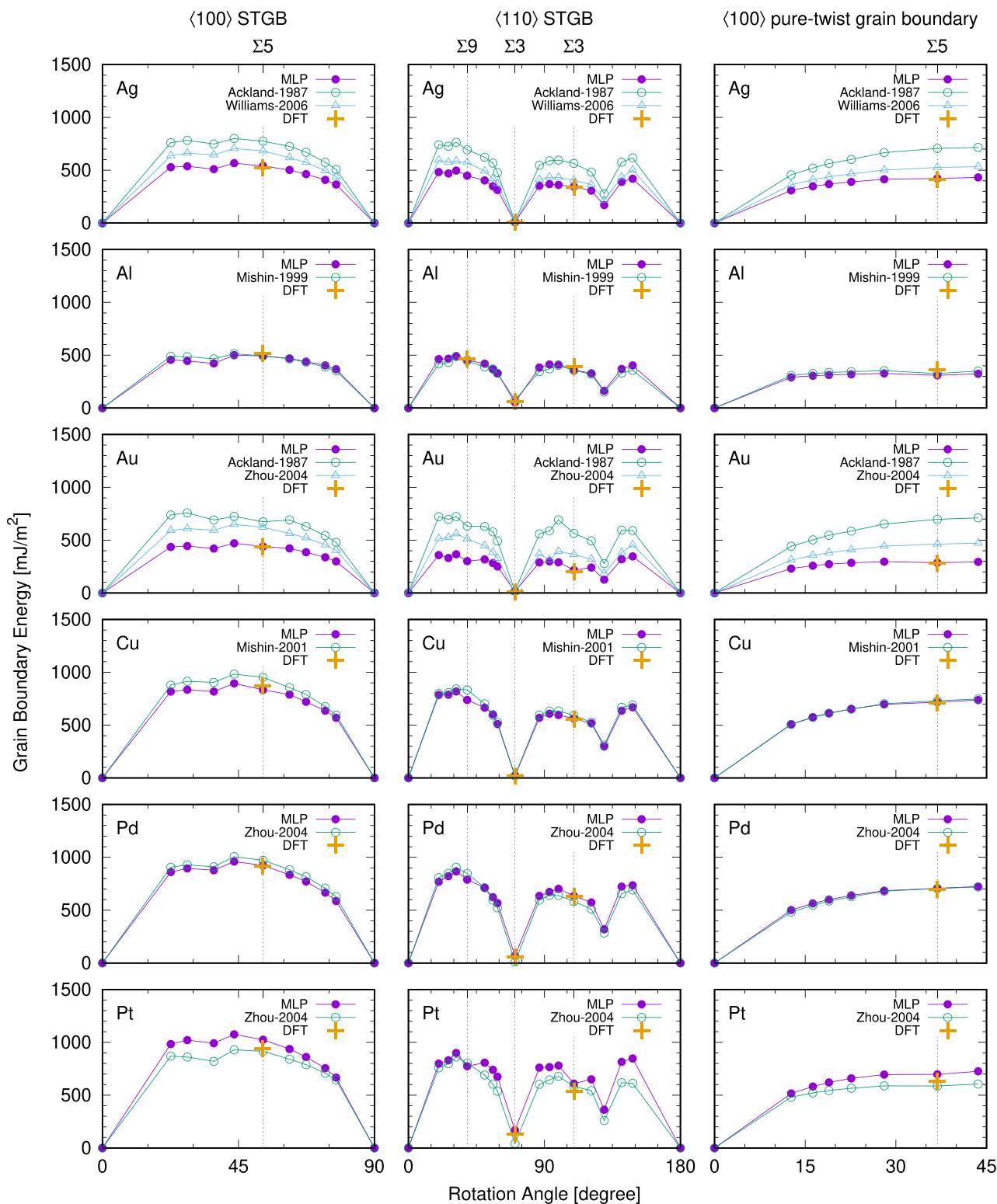
FIG. 3. Rotation angle dependence of the grain boundary energy for ⟨100⟩ STGBs, ⟨110⟩ STGBs, and ⟨100⟩ pure-twist grain boundaries for elemental Ag, Al, Ag, Cu, Pd, and Pt, predicted using the MLPs. For comparison, the grain boundary energies predicted using EAM potentials for Ag [58,59], Al [60], Au [58,61], Cu [62], Pd [61], and Pt [61] are shown by open symbols. The grain boundary energies computed by DFT calculation are also shown by crosses.

fcc elemental metals Ag, Al, Au, Cu, Pd, and Pt. In every elemental metal, the values of the grain boundary energy computed using the MLP are consistent with those computed by DFT calculation. We emphasize that the training datasets used to develop the MLPs contain no grain boundary structures. Therefore, the consistency indicates that the MLPs have high predictive power for the grain boundary structures and their energies. The present results also imply that the MLPs

in the repository, including those for other systems, should be useful in accurately predicting grain boundary properties and other complex defect properties.

APPENDIX A: POTENTIAL ENERGY MODELS

This section summarizes potential energy models used for developing MLPs in the Machine Learning Potential Repository [47]. In MLPs of the repository, the short-range part of the total energy for a structure is expressed by the sum of the atomic energy. The atomic energy is given by a function of invariants for the O(3) group [50,67] as

$$E^{(i)} = F(d_1^{(i)}, d_2^{(i)}, \dots), \qquad (A1)$$

where $d_n^{(i)}$ denotes a structural feature or an invariant derived from order parameters representing the neighboring atomic density of atom i. In the repository, a set of structural features derived only from radial functions (feature type = pair) and a set of polynomial invariants of the O(3) group derived from radial and spherical harmonic functions (feature type = invariants) are employed for developing MLPs.

The repository uses polynomial functions as function F representing the relationship between the atomic energy and a given set of structural features, $D = \{d_1, d_2, \dots\}$. The polynomial functions with regression coefficients $\{w\}$ are given

as follows:

$$F_1(D) = \sum_i w_i d_i$$

$$F_2(D) = \sum_{\{i,j\}} w_{ij} d_i d_j \qquad (A2)$$

$$F_3(D) = \sum_{\{i,j,k\}} w_{ijk} d_i d_j d_k$$

$$\vdots$$

A potential energy model is identified with a combination of the polynomial functions and structural features.

In this paper, MLPs with the following four types of the potential energy model are selected as listed in Table I, although six types of the potential energy model have been introduced in the repository. When a set of pairwise structural features is described as $D_{\text{pair}}^{(i)}$, the model (model type = 2, feature type = pair) is a polynomial of the pairwise structural features with their cross terms, expressed as

$$E^{(i)} = F_1(D_{\text{pair}}^{(i)}) + F_2(D_{\text{pair}}^{(i)}) + F_3(D_{\text{pair}}^{(i)}) + \cdots. \qquad (A3)$$

The other three models are derived from the polynomial invariants. A set of the polynomial invariants is expressed by the union of sets of pth-order polynomial invariants $D_p^{(i)}$ as

$$D^{(i)} = D_{\text{pair}}^{(i)} \cup D_2^{(i)} \cup D_3^{(i)} \cup D_4^{(i)} \cup \cdots. \qquad (A4)$$

The model (model type = 2, feature type = invariants) is given by a polynomial of the polynomial invariants as

$$E^{(i)} = F_1(D^{(i)}) + F_2(D^{(i)}) + F_3(D^{(i)}) + \cdots. \qquad (A5)$$

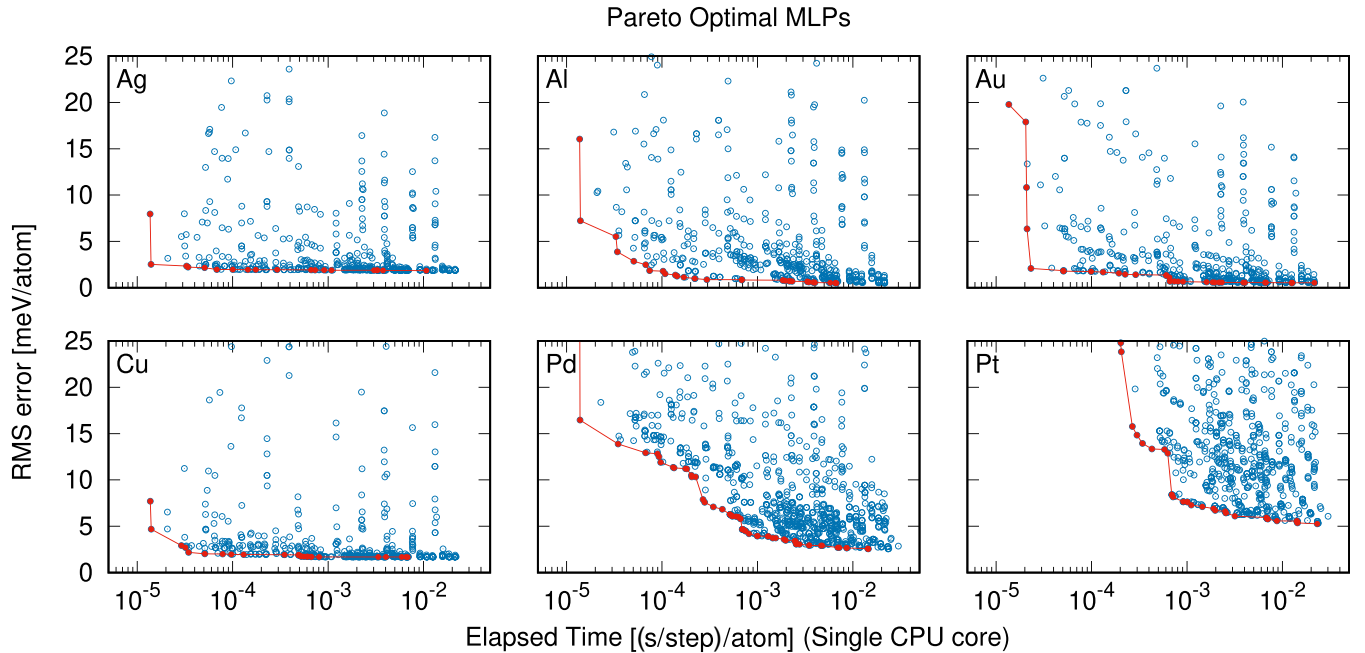The model (model type = 3, feature type = invariants) is the sum of a linear polynomial form of

FIG. 4. Distribution of MLPs for Ag, Al, Au, Cu, Pd, and Pt [47]. The elapsed time for a single point calculation is estimated using a single core of Intel® Xeon® E5-2695 v4 (2.10 GHz). The closed red circles show the Pareto optimal points of the distribution.

the polynomial invariants and a polynomial of pairwise structural features, described as

$$E^{(i)} = F_1(D^{(i)}) + F_2(D_{\text{pair}}^{(i)}) + F_3(D_{\text{pair}}^{(i)}) + \cdots . \quad (A6)$$

The model (`model type = 4, feature type = invariants`) is the sum of a linear polynomial form of the polynomial invariants and a polynomial of pairwise structural features and second-order polynomial invariants. This is written as

$$E^{(i)} = F_1(D^{(i)}) + F_2(D_{\text{pair}}^{(i)} \cup D_2^{(i)}) + \cdots . \quad (A7)$$

APPENDIX B: PARETO OPTIMALITY

Figure 4 shows the Pareto optimal MLPs for elemental Ag, Al, Au, Cu, Pd, and Pt. The distribution of MLPs is obtained by a systematic grid search to find optimal parameters controlling the accuracy and computational efficiency. The prediction error is estimated using the root mean square (RMS) error of the energy for the test dataset. The computational efficiency is estimated using the elapsed time to compute the energy, the forces, and the stress tensors of a structure with 284 atoms. The prediction error converges more slowly than the grain boundary energy, which originates from the fact that the prediction error is estimated from the test dataset composed of a wider variety of structures.

[1] A. P. Sutton and R. W. Balluffi, *Interfaces in Crystalline Materials* (Clarendon, Oxford 1995).

[2] J. Bishop and R. Hill, London, Edinburgh, Dublin Philos. Mag. J. Sci. **42**, 414 (1951).

[3] E. Kröner, Acta Metall. **9**, 155 (1961).

[4] Y. Mishin, M. Asta, and J. Li, Acta Mater. **58**, 1117 (2010).

[5] J. R. Greer and J. T. De Hosson, Prog. Mater. Sci. **56**, 654 (2011).

[6] G. C. Hasson and C. Goux, Scr. Metall. **5**, 889 (1971).

[7] D. Wolf, Scr. Metall. **23**, 1713 (1989).

[8] K. L. Merkle and D. Wolf, MRS Bull. **15**, 42 (1990).

[9] M. W. Finnis and J. E. Sinclair, Philos. Mag. A **50**, 45 (1984).

[10] M. S. Daw and M. I. Baskes, Phys. Rev. B **29**, 6443 (1984).

[11] J. W. Cahn, Y. Mishin, and A. Suzuki, Philos. Mag. **86**, 3965 (2006).

[12] S. von Alfthan, K. Kaski, and A. P. Sutton, Phys. Rev. B **74**, 134101 (2006).

[13] J. A. Brown and Y. Mishin, Phys. Rev. B **76**, 134118 (2007).

[14] M. Dao, L. Lu, R. J. Asaro, J. T. De Hosson, and E. Ma, Acta Mater. **55**, 4041 (2007).

[15] M. A. Tschopp and D. L. McDowell, Philos. Mag. **87**, 3147 (2007).

[16] D. L. Olmsted, S. M. Foiles, and E. A. Holm, Acta Mater. **57**, 3694 (2009).

[17] M. D. Sangid, H. Sehitoglu, H. J. Maier, and T. Niendorf, Mater. Sci. Eng. A **527**, 7115 (2010).

[18] M. A. Tschopp, K. N. Solanki, F. Gao, X. Sun, M. A. Khaleel, and M. F. Horstemeyer, Phys. Rev. B **85**, 064108 (2012).

[19] M. A. Tschopp, S. P. Coleman, and D. L. McDowell, Integr. Mater. Manuf. Innovation **4**, 176 (2015).

[20] S. Kiyohara, H. Oda, T. Miyata, and T. Mizoguchi, Sci. Adv. **2**, e1600746 (2016).

[21] G. S. Rohrer, E. A. Holm, A. D. Rollett, S. M. Foiles, J. Li, and D. L. Olmsted, Acta Mater. **58**, 5063 (2010).

[22] E. A. Holm, G. S. Rohrer, S. M. Foiles, A. D. Rollett, H. M. Miller, and D. L. Olmsted, Acta Mater. **59**, 5250 (2011).

[23] P. Hohenberg and W. Kohn, Phys. Rev. **136**, B864 (1964).

[24] W. Kohn and L. J. Sham, Phys. Rev. **140**, A1133 (1965).

[25] S. Lorenz, A. Groß, and M. Scheffler, Chem. Phys. Lett. **395**, 210 (2004).

[26] J. Behler and M. Parrinello, Phys. Rev. Lett. **98**, 146401 (2007).

[27] A. P. Bartók, M. C. Payne, R. Kondor, and G. Csányi, Phys. Rev. Lett. **104**, 136403 (2010).

[28] J. Behler, J. Chem. Phys. **134**, 074106 (2011).

[29] J. Han, L. Zhang, R. Car, and W. E, Commun. Comput. Phys. **23**, 629 (2018).

[30] N. Artrith and A. Urban, Comput. Mater. Sci. **114**, 135 (2016).

[31] N. Artrith, A. Urban, and G. Ceder, Phys. Rev. B **96**, 014112 (2017).

[32] W. J. Szlachta, A. P. Bartók, and G. Csányi, Phys. Rev. B **90**, 104108 (2014).

[33] A. P. Bartók, J. Kermode, N. Bernstein, and G. Csányi, Phys. Rev. X **8**, 041048 (2018).

[34] Z. Li, J. R. Kermode, and A. De Vita, Phys. Rev. Lett. **114**, 096405 (2015).

[35] A. Glielmo, P. Sollich, and A. De Vita, Phys. Rev. B **95**, 214302 (2017).

[36] A. Seko, A. Takahashi, and I. Tanaka, Phys. Rev. B **90**, 024101 (2014).

[37] A. Seko, A. Takahashi, and I. Tanaka, Phys. Rev. B **92**, 054113 (2015).

[38] A. Takahashi, A. Seko, and I. Tanaka, Phys. Rev. Mater. **1**, 063801 (2017).

[39] A. Thompson, L. Swiler, C. Trott, S. Foiles, and G. Tucker, J. Comput. Phys. **285**, 316 (2015).

[40] M. A. Wood and A. P. Thompson, J. Chem. Phys. **148**, 241721 (2018).

[41] C. Chen, Z. Deng, R. Tran, H. Tang, I.-H. Chu, and S. P. Ong, Phys. Rev. Mater. **1**, 043603 (2017).

[42] A. V. Shapeev, Multiscale Model. Simul. **14**, 1153 (2016).

[43] V. L. Deringer, C. J. Pickard, and G. Csányi, Phys. Rev. Lett. **120**, 156001 (2018).

[44] E. V. Podryabinkin, E. V. Tikhonov, A. V. Shapeev, and A. R. Oganov, Phys. Rev. B **99**, 064114 (2019).

[45] K. Gubaev, E. V. Podryabinkin, G. L. Hart, and A. V. Shapeev, Comput. Mater. Sci. **156**, 148 (2019).

[46] T. Mueller, A. Hernandez, and C. Wang, J. Chem. Phys. **152**, 050902 (2020).

[47] A. Seko, arXiv:2007.14206, https://sekocha.github.io/repository/index-e.html.

[48] S. Plimpton, J. Comput. Phys. **117**, 1 (1995).

[49] S. P. Ong, W. D. Richards, A. Jain, G. Hautier, M. Kocher, S. Cholia, D. Gunter, V. L. Chevrier, K. A. Persson, and G. Ceder, Comput. Mater. Sci. **68**, 314 (2013).

[50] A. Seko, A. Togo, and I. Tanaka, Phys. Rev. B **99**, 214108 (2019).

[51] P. E. Blöchl, Phys. Rev. B **50**, 17953 (1994).

[52] J. P. Perdew, K. Burke, and M. Ernzerhof, Phys. Rev. Lett. **77**, 3865 (1996).

[53] G. Kresse and J. Hafner, Phys. Rev. B **47**, 558 (1993).

[54] G. Kresse and J. Furthmüller, Phys. Rev. B **54**, 11169 (1996).

[55] G. Kresse and D. Joubert, Phys. Rev. B **59**, 1758 (1999).

[56] The computational time is estimated using a single core of Intel Xeon E5-2695 v4 (2.10 GHz).

[57] The DFT values of the grain boundary energy for $\Sigma 9$ STGB are missing in Ag, Au, Cu, Pd, and Pt. The electronic structure calculation failed to converge for some of the elements, and the structure optimization did not finish within a reasonably long time for the others.

[58] G. J. Ackland, G. Tichy, V. Vitek, and M. W. Finnis, Philos. Mag. A **56**, 735 (1987).

[59] P. L. Williams, Y. Mishin, and J. C. Hamilton, Model. Simul. Mater. Sci. Eng. **14**, 817 (2006).

[60] Y. Mishin, D. Farkas, M. J. Mehl, and D. A. Papaconstantopoulos, Phys. Rev. B **59**, 3393 (1999).

[61] X. W. Zhou, R. A. Johnson, and H. N. G. Wadley, Phys. Rev. B **69**, 144113 (2004).

[62] Y. Mishin, M. J. Mehl, D. A. Papaconstantopoulos, A. F. Voter, and J. D. Kress, Phys. Rev. B **63**, 224106 (2001).

[63] The computational cost of the EAM potential for Al is estimated to be 2×10^{-3} (ms/step)/atom.

[64] J. Li, Model. Simul. Mater. Sci. Eng. **11**, 173 (2003).

[65] W. T. Read and W. Shockley, Phys. Rev. **78**, 275 (1950).

[66] G. Simmons and H. Wang, *Single Crystal Elastic Constants and Calculated Aggregate Properties: A Handbook*, 2nd ed. (MIT Press, Cambridge, 1971).

[67] A. P. Bartók, R. Kondor, and G. Csányi, Phys. Rev. B **87**, 184115 (2013).